RSC Advances

ROYAL SOCIETY OF CHEMISTRY

PAPER



Cite this: *RSC Adv.*, 2021, **11**, 16881

# How to identify a smoker: a salient crystallographic approach to detect thiocyanate content†

Khushboo Iman, ‡[a] M. Naqi Ahamad, ‡[a] Monika,[b] Azaj Ansari,[b] Hatem A. M. Saleh,[a] M. Shahnawaz Khan,[a] Musheer Ahmad,[c] Rosenani A. Haque[d] and M. Shahid *[a]

There is an increasing demand for monitoring environmental pollutants and the control requires new sensing materials with better sensitivity, selectivity and reliability. In this study, a series of $Co_7$ clusters incorporating various flexible polyhydroxyamine ligands are explored, with the first report of thiocyanate recognition triggered by crystal formation using a $Co_7$ crystal (**1**). For this, we have fortunately synthesized three new mixed metal $Co_7$ clusters with fascinating structural features. The clusters were characterized by spectroscopic and single crystal X-ray diffraction methods and later by DFT calculations. Due to its better emission spectrum, **1** was further utilized for evaluating its sensing ability towards various anions in water. Surprisingly, **1** shows better quenching ability towards the recognition of $SCN^-$ with a better binding constant. The luminescence quenching towards $SCN^-$ detection was further verified by the single crystal method, HSAB principle (symbiosis) and theoretical calculations such as DFT studies. The SCXRD data clearly suggest that the $Co_7$ (**1**) can be converted into $Co_{14}$ (**1a**) by direct reaction with NaSCN under ambient conditions. Besides the soft/hard acid–base concept (symbiosis), the energies of formation, and Co–NCS and Co–$OH_2$ bond energies (as unravelled by DFT) are responsible for this transformation. Therefore, **1** can be used as a selective and sensitive sensor for the detection of thiocyanate anions based on the fluorescence amplification and quenching method. Further, the designed cluster has also been utilized to detect anions in human blood samples to differentiate a smoker and a non-smoker. It has been concluded that the samples of smokers have a high degree of thiocyanate (~12 or 9.5 mg $L^{-1}$) in comparison to those of non-smokers (2–3 mg $L^{-1}$). Thus, this kind of cluster material has high potentiality in the field of bio-medical science in future endeavours for identification of the extent of thiocyanate content in smokers.

Received 5th March 2021
Accepted 7th April 2021

DOI: 10.1039/d1ra01749g

rsc.li/rsc-advances

## 1. Introduction

Over the past two decades, the toxicological extent of thiocyanate has been clear as its toxicity is like cyanide, which has received much attention from researchers in various fields such as environmental science, food chemistry, and medicine.[1] Thiocyanate anion ($SCN^-$) is extracted from different sources, such as manufacturing processes, *e.g.* industrial wastewater, organism metabolites, pesticide residues, fabric dyeing, hydrometallurgy, electroplating, and photofinishing, tobacco smoke, diet and even car exhaust,[2] which presents a significant threat to the atmosphere and the human body as a result of its cumulative action. $SCN^-$ could be turned to extremely radioactive cyanide by irradiation and chlorination, resulting in serious health and environmental issues.[3] Tobacco smoke contains high concentrations of this ion and clinical tests have found that the concentration of saliva thiocyanate is greater for smokers than for non-smokers. Therefore, the thiocyanate concentration is known to be a successful test to differentiate between smokers and non-smokers.[4] In addition, $SCN^-$ appears to become a small metabolite of $CN^-$, the aggregation of which results from access to prolonged tobacco smoke.[5] Specifically, $SCN^-$ can effectively inhibit thyroid gland absorption of iodide ions, resulting in less thyroxine and iodide deficiency, which is more severe for pregnant women and babies.[6] In food analysis, the development of techniques for $SCN^-$ detection has gained substantial interest. For the detection of $SCN^-$, there are several techniques such as voltammetry,[7] ion chromatography,[8,9]

[a]*Functional Inorganic Materials Lab (FIML), Department of Chemistry, Aligarh Muslim University, Aligarh 202002, India. E-mail: shahid81chem@gmail.com*

[b]*Department of Chemistry, Central University of Haryana, Mahendergarh 123031, Haryana, India*

[c]*Department of Applied Chemistry (ZHCET), Aligarh Muslim University, Aligarh 202002, India*

[d]*School of Chemical Sciences, Universiti Sains Malaysia, USM, 11800, Penang, Malaysia*

† Electronic supplementary information (ESI) available. CCDC 2005498–2005500. For ESI and crystallographic data in CIF or other electronic format see DOI: 10.1039/d1ra01749g

‡ These authors contributed equally.

capillary zone electrophoresis,[10] high performance liquid chromatography (HPLC),[11] flow injection analysis,[12] fluorescence approaches,[13–15] colorimetry,[16–18] and surface-enhanced Raman scattering (SERS).[19,20] While these methods are quite useful for SCN-detection, several of them need sophisticated instruments, time-consuming methods, technical expertise and even costly or toxic reagents for sample pre-treatment. In addition, some of them eventually interact with some other coexisting anions. Therefore, it is very important to establish a simple, quick and sensitive method for the detection of SCN. Biomonitoring is an emerging area that combines environmental monitoring and public health surveillance. It involves the collection of samples of human biospecimens such as blood, saliva, or urine for measuring human exposure to chemical substances. Biomarkers are defined as an indicator of a certain physiological or pathophysiological condition for the purpose of biomonitoring. Thiocyanate anion, a detoxification product of cyanide in urine, saliva and blood, is a biomarker of exposure to tobacco smoke components and distinguishes smokers from non-smokers. Thiocyanate ion is naturally present in human body fluids and its concentration varies according to diet but its high concentration exhibits an evil effect among other factors, which is characterized by a relatively long half-life in the human body, *i.e.*, 6 days.[21] But its concentration increases when there is an exposure to cyanide. It has been found that smokers have significantly higher amounts of SCN in their urine and saliva than non-smokers. The concentration of thiocyanate ion in the saliva of non-smokers ranges between 0.5 and 2 mM, while in smokers concentrations as high as 6 mM can be found.[1] In this manuscript, we present three mixed-valent heptanuclear cobalt clusters (**1**, **2** and **3**) (Scheme 1) designed by the use of three different flexible polyhyrdoxylamine ligands *viz.* tris(hydroxymethyl)amino methane ($H_3L^1$), {2-[bis(2-hydroxyethyl) amino]-2-(hydroxymethyl) propane-1,3-diol} ($H_6L^2$) and 2-amino-2-methyl-1,3-propanediol ($H_2L^3$) respectively, acting as multidentate ligands (Scheme 2) and NaSCN as an auxiliary ligand. The clusters thus obtained, $[Co_4^{II}Co_3^{III}(H_3L^1)_5(\mu_2\text{-}O)_6(\mu_3\text{-}O)_6(NCS)_5H_2O]$ (**1**), $[Co_4^{II}Co_3^{III}(H_6L^2)_3(\mu_2\text{-}O)_6(\mu_3\text{-}O)_6(NCS)_6]$ (**2**) and $[Co^{II}_4Co^{III}_3(L^3)_6(\mu_2\text{-}O)_6(\mu_3\text{-}O)_6(NCS)_6]$ (**3**), contain a similar $Co_7$ core. Coordination of ligands is almost similar in such a way that **2** and **3** are alike and comprise 6 Co–NCS bonds while **1** differs comparatively, ligated by 5 NCS and 1 $H_2O$ molecule to peripheral cobalt centres. We take advantage of this peculiar feature and successfully replaced the water molecule in **1** with NaSCN. Consequently, reaction of **1** with SCN results in the NaSCN (guest) induced monomeric ($Co_7$) to sodium bridged dimeric ($Co_{14}$) direct transformation, thus leading to the detection of thiocyanate by **1**.

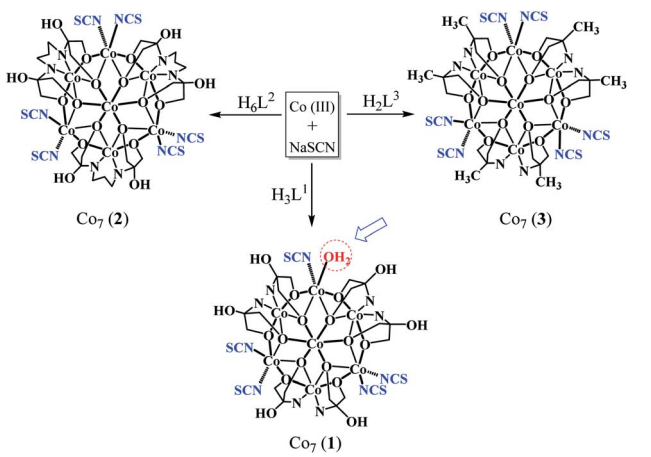


Scheme 1 Routes for the synthesis of heptanuclear mixed-valent cobalt clusters.

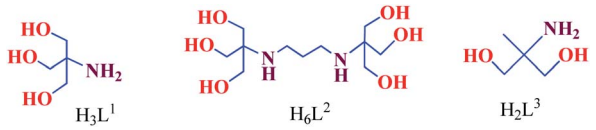


Scheme 2 Three different polyhydroxyl amine ligands used in $Co_7$ formation.

## 2. Experimental

### 2.1. Materials and methods

All reagents including $H_3L^1$, $H_6L^2$, $H_2L^3$, NaOH, NaSCN, $CoCl_2\cdot 6H_2O$ and $Co(OAc)_2\cdot 4H_2O$ are of analytical grade which have been purchased from Sigma-Aldrich Chemical Co., India, and are used without further purification. All experiments were performed in compliance with the authors' institute's policy on animal use and ethics.

### 2.2. Physical methods

The FTIR spectra of the compounds were recorded within the range 4000–400 $cm^{-1}$ using KBr pellets on a PerkinElmer Model spectrum GX spectrophotometer. Fluorescence measurements are made on a Hitachi F-2700 spectrophotometer. The electronic absorption spectra (900–200 nm) of the complexes are recorded at room temperature using a PerkinElmer Lambda-45 UV-vis spectrophotometer, with cuvettes of 1 cm path length. PXRD patterns have been recorded with a "Miniflexll X-ray diffractometer" with Cu-K$\alpha$ radiation. Single crystal X-ray diffraction of the complexes was performed at 296 K on a Bruker SMART APEX CCD diffractometer. Thermal gravimetric analysis (TGA) data are measured from room temperature to 550 °C at a heating rate of 20 °C $min^{-1}$. A Shimadzu TGA-50H instrument is used for the TGA data collection.

### 2.3. Computational details

All the calculations were computed using Gaussian 09 program.[22] A fragmentation approach is available in Gaussian which was used for the calculations. From our previous studies,[23–25] we concluded that the B3LYP-D2[26–28] functional is the most suitable functional for the spin states and the energetics; thus, here we have confined our calculations on the B3LYP-D2 functional incorporating dispersion correction of Grimme *et al.* The LACVP basis set comprising the LanL2DZ Los Alamos effective core potential for Co[29–31] and a 6-31G[32,33] basis

set for the other atoms (hydrogen, carbon, nitrogen, oxygen and sulphur) was used for the single point calculations.

### 2.4. X-ray crystal structure determination and refinements

Single-crystal X-ray data of **1**, **2** and **1a** are collected at 100 or 298 K on a Bruker SMART APEX CCD diffractometer using graphite monochromated Mo-Kα radiation ($\lambda = 0.71073$ Å). The crystal structure data were collected using graphite monochromated Mo-Kα radiation ($\lambda = 0.71073$ Å). The international X-ray crystallography tables have taken the linear absorption coefficients, the dispersion factors of the atoms, and the unusual dispersion corrections.[34] SAINT software has been used to facilitate data integration and reduction.[35] The collected reflections were corrected by empirical absorption with SADABS,[36] and an XPREP determination of the complex space group was carried out. Both of the structures were refined using Olex2.Refine[37–39] and solved with SIR-97.[39] The complex solution was performed using the direct solution method. CCDC reference numbers for **1**, **2** and **1a** are, respectively, 2005500, 2005499 and 2005498.†

### 2.5. Designing of 1–3

**2.5.1. Synthesis of $[Co_4^{II}Co_3^{III}(H_3L^1)_5(\mu_2\text{-}O)_6(\mu_3\text{-}O)_6(NCS)_5H_2O]$ (1).** A solution of cobalt acetate tetrahydrate (0.177 g, 1 mmol) in a 95 : 5 v/v MeOH : $H_2O$ mixture (10 mL) is added to a solution of $H_3L^1$ (0.121 g, 1 mmol) in a 95 : 5 v/v MeOH : $H_2O$ mixture (25 mL), which turns the colorless solution into blue. After stirring for 1 h, methanolic solution of sodium thiocyanate (0.081 g, 1 mmol) is added to give a purple color solution and the resultant solution is stirred for 6 h at room temperature. Slow evaporation of the solvent at room temperature led to the formation of purple block-shaped crystals suitable for single-crystal X-ray diffraction within a period of 25 days.

Anal calc. (%): C 24.37, H 3.38, N 9.80; found for $C_{29}H_{48}Co_7N_{10}O_{20}S_5$: C 24.44, H 3.35, N 9.76. TGA: temperature range/°C (weight loss%): 20–250 (5.10%); 250–460 (34%); 460–550 (39.39%). FTIR spectra (KBr pellets, $cm^{-1}$): $\nu(H_2O)$: 3469, 3416; $\nu$(SCN): 2070; $\nu$(O–H): 3416 $\nu$(C–H): 2865; $\nu$(C–O): 1639, 1617; $\nu(NH_2)$: 3242, $\nu$(Co–O–Co): 807, 928.

**2.5.2. Synthesis of $[Co_4^{II}Co_3^{III}(H_6L^2)_3(\mu_2\text{-}O)_6(\mu_3\text{-}O)_6(NCS)_6]$ (2).** A solution of cobalt chloride hexahydrate (0.474 g, 2 mmol) in methanol (25 mL) is added to a colorless solution of $H_6L^2$ (0.282 g, 1 mmol) in methanol (25 mL), which turns the colorless solution into blue. After stirring for 1 h, methanolic solution of sodium thiocyanate (0.081 g, 1 mmol) is added dropwise to give a purple color solution and the resultant solution is stirred for 6 h at room temperature. Slow evaporation of the solvent at room temperature led to the formation of red colored fine crystals suitable for single-crystal X-ray diffraction within a period of one month.

Anal calc. (%): C 28.88, H 3.73, N 10.36; found for $C_{39}H_{60}Co_7N_{12}O_{20}S_6$: C 28.51, H 3.30, N 9.66. TGA: temperature range/°C (weight loss%): 20–250 (8.8%); 250–500 (36.22%); 500–600

Table 1 Crystal data and structure refinement parameters of the complexes

| Empirical formula | $C_{29}H_{49}Co_7N_{11}O_{22}S_5$ (**1**) | $C_{60}H_{112}Co_{14}N_{24}Na_2O_{48}S_{12}$ (**1a**) | $C_{38}H_{64}Co_7N_{12}O_{18.5}S_6$ (**2**) |
|---|---|---|---|
| Formula weight | 1476.64 | 3193.53 | 1621.91 |
| Temperature/K | 100(2) | 100(2) | 100(2) |
| Crystal system | Monoclinic | Triclinic | Triclinic |
| Space group | $P2_1/n$ | $P\bar{1}$ | $P\bar{1}$ |
| $a$/Å | 10.4402(5) | 10.6166(4) | 12.3559(8) |
| $b$/Å | 22.5053(11) | 13.9034(5) | 12.4348(8) |
| $c$/Å | 22.5028(11) | 19.5343(6) | 20.8341(13) |
| $\alpha$/° | 90 | 94.8730(10) | 82.586(2) |
| $\beta$/° | 90.962(2) | 102.5290(10) | 81.206(2) |
| $\gamma$/° | 90 | 92.8500(10) | 68.792(2) |
| Volume/Å$^3$ | 5286.5(4) | 2797.67(17) | 2939.7(3) |
| $Z$ | 4 | 1 | 1 |
| $\rho_{calc}$, g cm$^{-3}$ | 1.8552 | 1.8954 | 1.7961 |
| $\mu$/mm$^{-1}$ | 2.423 | 2.343 | 2.216 |
| $F$(000) | 2993.6 | 1623.2 | 1625.0 |
| Crystal size/mm$^3$ | 0.31 × 0.2 × 0.15 | 0.36 × 0.23 × 0.14 | 0.47 × 0.38 × 0.19 |
| Radiation | Mo Kα ($\lambda = 0.71073$) | Mo Kα ($\lambda = 0.71073$) | Mo Kα ($\lambda = 0.71073$) |
| $2\theta$ range for data collection/° | 4.28 to 50.1 | 5.08 to 50.1 | 5.02 to 50.1 |
| Index ranges | $-13 \le h \le 13$, $-30 \le k \le 30$, $-29 \le l \le 29$ | $-14 \le h \le 14$, $-18 \le k \le 18$, $-25 \le l \le 26$ | $-16 \le h \le 16$, $-16 \le k \le 16$, $-27 \le l \le 27$ |
| Reflections collected | 82 786 | 45 252 | 48 182 |
| Independent reflections | 9357 [$R_{int} = 0.0945$, $R_{sigma} = 0.0643$] | 9901 [$R_{int} = 0.0662$, $R_{sigma} = 0.0711$] | 10 401 [$R_{int} = 0.0407$, $R_{sigma} = 0.0438$] |
| Data/restraints/parameters | 9357/0/680 | 9901/0/731 | 10 401/0/758 |
| Goodness-of-fit on $F^2$ | 1.095 | 1.048 | 1.046 |
| Final $R$ indexes [$I \ge 2\sigma(I)$] | $R_1 = 0.0535$, w$R_2 = 0.1338$ | $R_1 = 0.0501$, w$R_2 = 0.1150$ | $R_1 = 0.0784$, w$R_2 = 0.2110$ |
| Final $R$ indexes [all data] | $R_1 = 0.0768$, w$R_2 = 0.1572$ | $R_1 = 0.0696$, w$R_2 = 0.1297$ | $R_1 = 0.0877$, w$R_2 = 0.2202$ |
| Largest diff. peak/hole/e Å$^{-3}$ | 2.00/−2.10 | 2.41/−1.24 | 3.18/−3.28 |

(29.30%). FTIR spectra (KBr pellets, $cm^{-1}$): $\nu$(O–H): 3240, 3518; $\nu$(C–H): 2436; $\nu$(SCN): 2075; $\nu$(C–O): 1646; $\nu(NH_2)$: 3216; $\nu$(Co–O–Co): 945 and 825.

**2.5.3. Synthesis of $[Co^{II}_4Co^{III}_3(L^3)_6(\mu_2\text{-}O)_6(\mu_3\text{-}O)_6(NCS)_6]$ (3).** 3 was synthesized adopting the procedure already reported in the literature.[33] Slow stirring of $H_3L^3$ (5 mmol) and 10 mmol NaSCN for ten minutes in methanol produced a clear colourless solution. To this solution was added dropwise methanolic solution (5 mL) of 10 mmol $Co(NO_3)_2$ or $Co(OAc)_2$ under aerobic conditions. After 2 h of stirring the brown solution was kept overnight which afforded reddish brown crystals of 3.

# 3. Results and discussion

## 3.1. Description of crystal structures

Single crystal X-ray data (Table 1) reveal that **1** crystallizes in the monoclinic space group $P2_1/n$ to give a mixed-valence heptanuclear cobalt complex $[Co_7(H_3L^1)_6(\mu_2\text{-}O)_6(\mu_3\text{-}O)_6(NCS)_5H_2O]$ (Fig. 1). The star shaped metal core is formed by the bridging of six $\mu_2$-alkoxo groups between six cobalt ions on the rim which are linked to the central cobalt ion through six $\mu_3$-alkoxy bridging groups, resulting in a structure which is best described as a wheel-shaped disc like structure. $Co_1$ and $Co_3$ on the rim adopt $CoN_2O_4$ configuration ligated by two NCS, two $\mu_2$-alkoxo groups and two $\mu_3$-alkoxy groups each. $Co_5$ adopts $CoNO_5$ configuration ligated by one NCS, one water molecule, two $\mu_2$-alkoxo groups and two $\mu_3$-alkoxy groups. $Co_2$, $Co_4$ and $Co_6$ adopt $CoN_2O_4$ configuration ligated by two $H_3L^1$, two $\mu_2$-alkoxo groups and two $\mu_3$-alkoxy groups. The central cobalt ion $Co_7$ is ligated by six $\mu_3$-alkoxy groups. All the cobalt centres have a distorted octahedron geometry. The asymmetric unit of **1** consists of one complete $[Co_7(H_3L^1)_6(\mu_2\text{-}O)_6(\mu_3\text{-}O)_6(NCS)_5H_2O]$ unit, two water molecules and one free oxygen atom. Bond-valence sum calculations (Table S1†) and charge consideration establish that $Co_1$, $Co_3$, $Co_5$ and $Co_7$ are in the +2 oxidation state while $Co_2$, $Co_4$ and $Co_6$ are in the +3 oxidation state. Moreover, the hydrogen atoms of the coordinated $H_3L^1$ in **1** form moderately strong hydrogen bonds (C4–H1b···O6 = 2.422 Å; C18–H18···O4 = 2.704 Å; O4–H4···O17 = 2.161 Å) with the acceptor oxygen atoms of neighboring $H_3L^1$. The packing features of **1** reveal a 1D chain as a result of non-covalent interactions as illustrated in Fig. S1 and S2.† **2** crystallizes in the triclinic space group $P\bar{1}$ to give a mixed-valence heptanuclear cobalt complex, $[Co_7(H_6L^2)_3(\mu_2\text{-}O)_6(\mu_3\text{-}O)_6(NCS)_6]$ (Fig. 1). All the cobalt centers have a distorted octahedral geometry. The asymmetric unit of **2** is similar to that of **1** and consists of one complete unit of $[Co_7(H_6L^2)_3(\mu_2\text{-}O)_6(\mu_3\text{-}O)_6(NCS)_6]$ (Fig. 1) and two lattice water. Bond-valence sum calculations confirm $Co_3$, $Co_4$ and $Co_7$ to be in +3 the oxidation state while $Co_1$, $Co_2$, $Co_5$ and $Co_6$ in the +2 state (Table S1†). Moreover, the coordinated $H_6L^2$ in **2** forms strong hydrogen bonds (O031–H031···O026 = 1.873 Å) with the acceptor oxygen atoms of neighboring $H_6L^2$. The packing diagram of **2** indicates the existence of a 2D sheet due to the non-covalent interactions (Fig. S1 and S3†). The crystal structure of **3** *i.e.*, $[Co^{II}_4Co^{III}_3(L^3)_6(\mu_2\text{-}O)_6(\mu_3\text{-}O)_6(NCS)_6]$ is already given in our earlier report[33] (Fig. 1), so there is no need to discuss it here and this complex has been taken into consideration for comparison purpose only.[40,41]

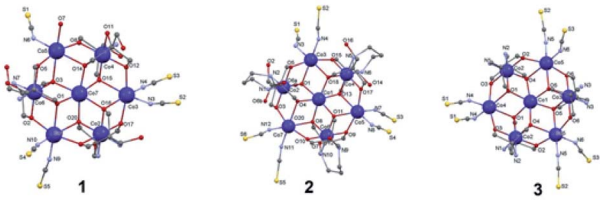


Fig. 1 Molecular structures of **1**, **2**, **3**.

## 3.2. FTIR and thermal gravimetric analysis (TGA) and PXRD pattern of 1–3

The colored crystals of the compounds are given in Fig. 2a. Bands due to the coordinated $H_3L^1$ and $H_6L^2$ ligands are investigated in many regions. Metal complexes exhibit bands at approximately 3412 $cm^{-1}$ (**1**) and 3468 $cm^{-1}$ (**2**) due to $\nu$(O–H) stretching vibrations. Broad bands at approximately at 3242 $cm^{-1}$ (**1**) and 3216 $cm^{-1}$ (**2**) correspond to $\nu(NH_2)$ stretching vibrations. The broad nature of these bands can be attributed to the presence of hydrogen bonding interactions. The $\nu$(C–H) stretching vibrations occur as several medium to weak intensity bands at 2900 $cm^{-1}$. The presence of the $CH_2$ group is further verified from the observed $CH_2$ bending frequency at 1450 $cm^{-1}$. The bands appearing in the 1639 and 1617 region are characteristic of $\nu$(C–O) for **1** and **2**. Further, **1** and **2** exhibit a sharp peak approximately at 2070 and 2071, attributed to $\nu(SCN^-)$ stretching vibrations. The bands appearing around 945, 825 and 807, 928 $cm^{-1}$ are characteristic of a bridging M–O–M group in **1** and **2**. The bands observed in the low frequency region (430–520 $cm^{-1}$) are due to M–N and M–O stretching vibrations (Fig. 2b).[42] Thermal gravimetric analysis (TGA) is carried out under an $N_2$ atmosphere at a rate of 10 °C $min^{-1}$ to investigate the thermal fragmentation patterns of **1** and **2** (Fig. 2c). The thermogram for **1** shows that the complex eliminates water molecules at temperatures up to 200 °C. The % weight loss of 4% in the first step corresponds to the exact number of two lattices along with one coordinated water molecule present as proposed from the analytical data and crystal structures. Above this temperature, the complex

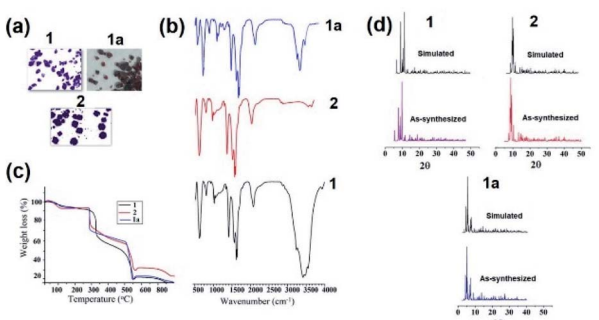


Fig. 2 (a) Crystals, (b) FTIR, and (c) TGA plots of **1**, **1a** and **2** respectively. (d) As-synthesized and simulated PXRD patterns of **1**, **2** and **1a**.

species undergo fragmentation in two more steps. In the second step, the removal of the four amino alcohol ligands takes place in the temperature range 250–460 °C, with a weight loss of 34%. A further increase in the temperature up to 550 °C gives rise to the elimination of coordinated thiocyanate ligands from the rest of the compound with a weight loss of 39%. Beyond the temperature of 550 °C, the rest of the metal oxide compound starts to decompose.[43] The thermogram for **2** shows that the complex eliminates thiocyanate ligands at temperatures up to 250 °C. The weight loss of 8% in this first step corresponds to the exact number of four coordinated thiocyanate ligands from the coordination sphere as proposed from the analytical data and crystal structures. Above this temperature, the complex species undergo fragmentation in two more steps. In the second step, the removal of the three amino alcohol ligands along with two thiocyanate ligands takes place in the temperature range 250–500 °C, with a weight loss of 36%. A further increase in the temperature up to 600 °C gives rise to the elimination of rest of the metal oxide compound from the rest of the compound with a weight loss of 29%. Moreover, the simulated and as-synthesized powder X-ray diffraction (PXRD) patterns are identical for the clusters, indicating bulk purity (Fig. 2d).

### 3.3. Sensing application of 1

**3.3.1. Detection of thiocyanate anions.** The emission spectra of $[Co_4^{II}Co_3^{III}(H_3L^1)_6(\mu_2\text{-}O)_6(\mu_3\text{-}O)_6(NCS)_5H_2O]$ (**1**) are investigated in different solvents such as $H_2O$, EtOH, MeCN and benzene (Fig. 3). 3 mg crystals of **1** was dipped into the different solvents for an hour and sonicated before recording their luminescence spectra. It is observed that the emission spectrum of **1** is more intense in water so we have performed our further experiment in water. Emission at 384 nm upon excitation at 304 nm in **1** could be assigned to the luminescence from the intra-ligand transition.[44] The bright-blue luminescence of **1** made us explore its potential application in selective sensing of thiocyanate anions. Photoluminescence (PL) titration was performed for **1** at various concentrations of $SCN^-$ ion. The PL spectra of **1** were recorded in the absence and presence of sodium thiocyanate (NaSCN). The concentration of thiocyanate was varied from $1 \times 10^{-10}$ to $15 \times 10^{-10}$ M and this level of concentration is the limit of detection (LOD). The emission

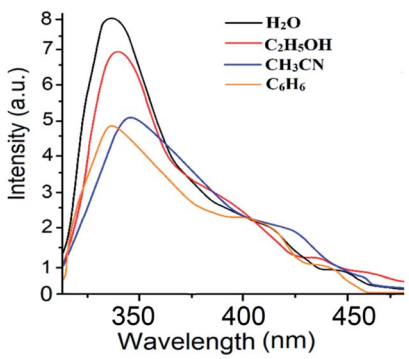


Fig. 3 Emission spectra of **1** dispersed in different solvents upon excitation at 304 nm.

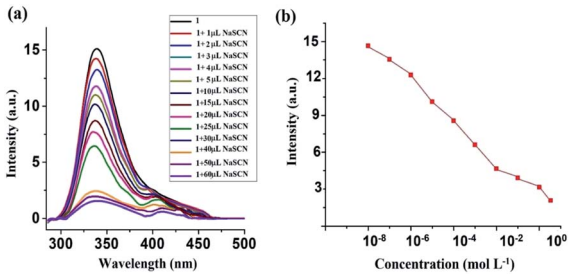


Fig. 4 (a) PL titration of thiocyanate ions with 1 and (b) PL intensity at 384 nm at various concentrations of the thiocyanate ion.

spectrum of **1** consists of a sharp peak at 384 nm. The PL intensity at 384 nm was quenched with the gradual addition of the thiocyanate anion (Fig. 4). **1** shows excellent sensing behavior towards thiocyanate anion by showing quenching of the initial fluorescence intensity by 92%.

**3.3.2. Binding constant.** The quenching phenomena are demonstrated by the Stern–Volmer (SV) plot using eqn (1).

$$\frac{F_0}{F} = 1 + K_{SV}[Q] \quad (1)$$

where $F_0$ and $F$ represent the fluorescence intensity of fluorophore **1** in the absence and presence of the quencher thiocyanate ions, respectively, $K_{SV}$ is the SV constant (or dynamic quenching constant) and [Q] is the quencher concentration. The SV plot (Fig. 5) shows a downward curvature toward the *x*-axis. Because of the nonlinearity of the plot, it is concluded that the quenching data do not follow the usual SV equation. Therefore, a modified SV equation (eqn (2)) has been used.

$$\frac{F_0}{F_0 - F} = \frac{1}{f_a} + \frac{1}{f_a K_a}\frac{1}{[Q]} \quad (2)$$

Here, $F_0$ and $F$ are the fluorescence intensities before and after the addition of the quencher, [Q] denotes the quencher concentration and $f_a$ is the fraction of the fluorophore accessible to the quencher. $K_a$ is the binding constant, which is obtained with the help of the intercept and slope (Fig. 5). The plot of $F_0/\Delta F$ *versus* 1/[Q] for the present fluorophore-quencher system gives rise to a straight line (Fig. 5), which gives rise to the binding constant ($K_a$). The value of $K_a$ is found to be 32.78 L mol$^{-1}$, which shows appreciable binding between the fluorophore and quencher.

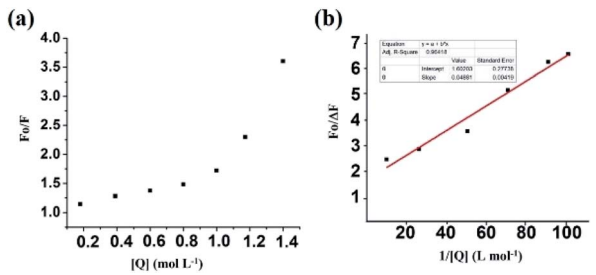


Fig. 5 (a) SV plot of the 1 in the presence of different thiocyanate ion concentrations. (b) Modified SV plot of **1** in the presence of NaSCN.

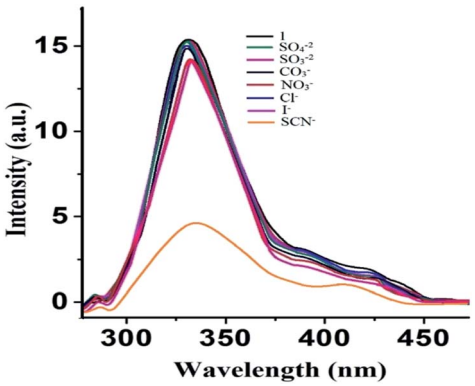


Fig. 6 Emission intensity of **1** towards various anions.

#### 3.3.3. Calculation of $K_a$ with respect to NaSCN.

$$\frac{F_0}{F_0 - F} = \frac{1}{f_a} + \frac{1}{f_a K_a}\frac{1}{[Q]}$$

From the plot, $x = 33.6$, $y = 3.24$; $3.24 = 1.6 + 1.6 \times 33.6 \times 1/K_a$; $1/K_a = 1.64/53.76$; $K_a = 32.78$.

**3.3.4. Selectivity study.** The study of selectivity of **1** (Fig. 6) towards the thiocyanate ion was assessed by taking 0.01 (M) concentration of different anions such as $SO_4^{2-}$, $SO_3^{2-}$, $CO_3^{-}$, $NO_3^{-}$, $Cl^{-}$ and $I^{-}$. The different anions were mixed with 1 mM concentration of **1**, and the mixture was subjected to a PL spectrometer. It was observed that there was no significant change in the spectra for all the anions with respect to the pure **1** except that of the thiocyanate ion.

Furthermore, to study any effects of the cationic part of the thiocyanate, potassium thiocyanate was taken with different concentrations. Interestingly, spectral behaviour as well as the binding constant has been found to be approximately the same as that of sodium thiocyanate (Fig. 7), which shows that there is no role of the cationic counterpart in the thiocyanate sensing process. Consequently, it may be concluded that **1** can sense thiocyanate ions selectively.

#### 3.3.5. Calculation of $K_a$ with respect to KSCN.

$$\frac{F_0}{F_0 - F} = \frac{1}{f_a} + \frac{1}{f_a K_a}\frac{1}{[Q]}$$

From the plot, $x = 51.82$, $y = 4.10$, $4.02 = 1.54 + 1.54 \times 51.82 \times 1/K_a$, $1/K_a = 2.48/79.80$, $K_a = 32.18$.

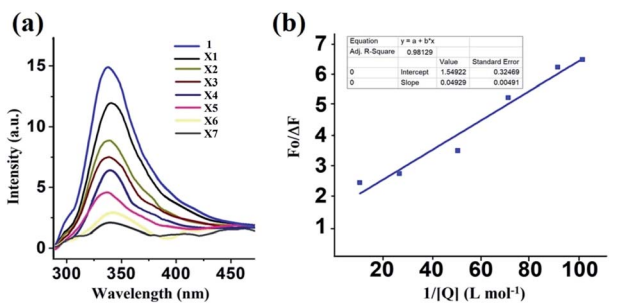


Fig. 7 (a) SV plot of the **1** in the presence of different KSCN ion concentrations. (b) Modified SV plot of **1** in the presence of KSCN.

#### 3.3.6. Thiocyanate recognition in the blood sample.

It has been examined that **1** can efficiently sense thiocyanate anions in synthetic solutions as well as real biological samples (Fig. 8). The results suggest that the quenching effect is more significant for the smoker blood samples (S1 and S2) compared to the non-smokers (NS1 and NS2). Therefore, **1** can act as a biomarker in the blood of smokers and non-smokers by differential quenching of fluorescence intensity.[45]

The comparative quenching effect reveals that the smoker blood contains more thiocyanate than its non-smoker counterpart. To evaluate the quantitative degree of smoking, a standard curve (PI *vs.* various synthetic solutions containing blood serum and a known amount of thiocyanate within 2–12 mg $L^{-1}$) has been plotted. Comparing the results of real samples with the standard curve, it has been concluded that the sample S2 has a high degree of thiocyanate (~12 mg $L^{-1}$) while sample S1 has a slightly low degree of thiocyanate (~9.5 mg $L^{-1}$). In contrast, the concentration of thiocyanate has been found in the range 2–3 mg $L^{-1}$ in the blood serum of non-smokers.

### 3.4 Mechanism of $SCN^-$ detection

To understand the mechanism behind the detection of $SCN^-$ in the aqueous medium, we have adopted three different methods to justify it. The first method involves the transformation of **1** into **1a** by simple reaction of **1** with NaSCN to form a suitable crystal for X-ray (Scheme 3). Secondly, we have performed the theoretical calculations to understand this transformation. Finally, the transformation can be easily defined by HSAB principle (symbiosis effect) as suggested in Scheme 4.

**3.4.1. Crystal formation, its characterization and single crystal X-ray analysis.** In a separate experimental setup, the transformation of $[Co_4^{II}Co_3^{III}(H_3L^1)_6(\mu_2\text{-}O)_6(\mu_3\text{-}O)_6(NCS)_5H_2O]$ (**1**) into $[\{Co_4^{II}Co_3^{III}(H_3L^1)_6Na(NCS)_5(\mu_2\text{-}O)_6(\mu_3\text{-}O)_6(\mu\text{-}NaSCN\{H_2O\}_3)\}_2\square 4H_2O$ (**1a**) has been carried out under ambient conditions. Purple colored single crystals of **1** are subjected to immersion into a 1 M aqueous solution of NaSCN which turned it into deep-purple color within a few minutes. The crystal did not dissolve and turned grayish-purple color after 5 minutes. The addition of NaSCN in the framework with simultaneous elimination of coordinated water is expected during the course

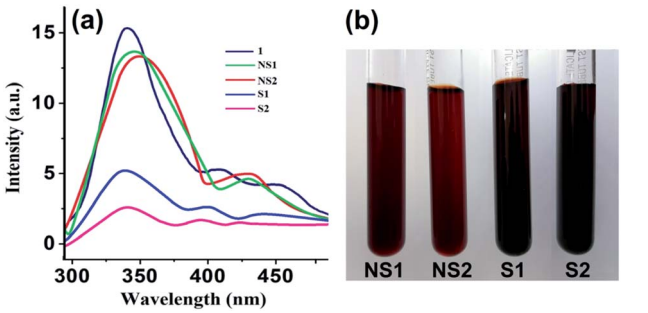


Fig. 8 (a) PL spectra of **1** in the smoker and the non-smoker blood samples (where NS and S stand for non-smoker and smoker, respectively) and (b) change in the colour of the blood after the addition of **1**.

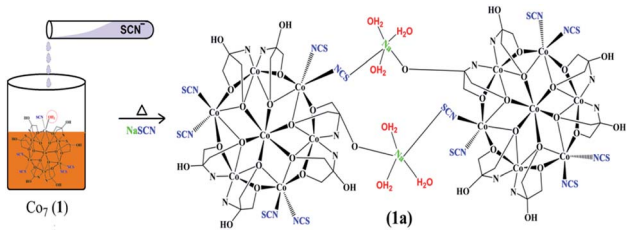


Scheme 3 Transformation of **1** into **1a** by addition of NaSCN.

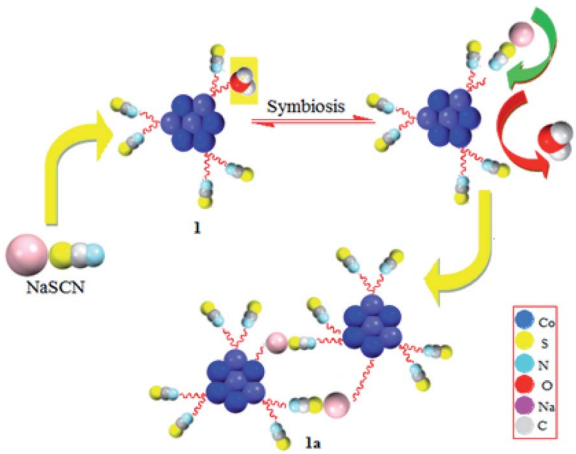


Scheme 4 Schematic representation of the transformation of **1a** by **1** *via* a chemical symbiosis effect.

of time. The obtained grayish-purple crystal of **1a** was analyzed crystallographically, which confirms the identity of the discrete mixed-valent $Co_{14}$ species, $[\{Co_4^{II}Co_3^{III}(H_3L^1)_6(NCS)_5(\mu_2\text{-}O)_6(\mu_3\text{-}O)_6(\mu\text{-}NaSCN\{H_2O\}_3)\}]_2$, which is a Na bridged-dimerized form of the monomeric unit of discrete mixed-valent heptanuclear $Co_7$ species, $[Co_4^{II}Co_3^{III}(H_3L^1)_6(\mu_2\text{-}O)_6(\mu_3\text{-}O)_6(NCS)_5H_2O]$. Surprisingly, the crystal structure of **1a** is significantly similar to that of **1**, despite the fact that it has a dimeric architecture bridged by NaSCN, having a different space group, colour and unit cell parameters (Scheme 3). Hence, **1** has been demonstrated as a reliable biomarker for thiocyanate anions. Smoking seems to centrifuge, which somehow throws people into health hazards. To tackle this troublesome problem, it is necessary to biomonitor toxic substances originating from tobacco smoke in biological materials sampled from persons with different exposures to tobacco smoke constituents. We present a transformation in which thiocyanate binds to the $[Co_4^{II}Co_3^{III}(H_3L)_6(SCN)_5H_2O]$ scaffold that induces the formation of the $[Co_4^{II}Co_3^{III}(H_3L)_6(SCN)_6]$ asymmetric complex and thereby triggers effective fluorescence quenching. Single-crystal X-ray diffraction of **1a** discloses that discrete monomer **1** ($Co_7$) transforms to a discrete Na bridged-dimer **1a** ($Co_{14}$) without alternation of each of the monomeric unit of the $Co_7$ core which are bridged by $\mu$-$Na(SCN)(H_2O)_3$. It crystallizes in the triclinic group $P\bar{1}$ (Table 1). The NaSCN molecule replaces $H_2O$ *via* simple transformation without changes of the core (Fig. 1).

Coordination mode around one cobalt ion in one monomeric unit that is coordinated to a water molecule gets replaced by the $\mu$-$Na(SCN)(H_2O)_3$ entity, which is further bound to the oxygen atom of $H_3L^1$ of another monomeric $Co_7$ unit to give a dimer like structure bridged by sodium cations. The asymmetric unit of **1a** consists of a $[\{Co_4^{II}Co_3^{III}(H_3L^1)_6(NCS)_5(\mu_2\text{-}O)_6(\mu_3\text{-}O)_6Na(\mu\text{-}Na(SCN)\{H_2O\}_3)\}]$ unit which is one half of the complete molecule of **1a**, and three free water molecules. Interestingly, Na–S is a weak bond which is a bit longer (3.013(5) Å), but taking it as a bong cannot be ruled out. Bond Valence Sum (BVS) analysis also suggests it to be weaker than the Na–O bonds, but definitely significant. This molecule (**1a**) is a rare example of existence of a longer Na–S bond and sodium bridging consolidating the two $Co_7$ units together just as the bonding rods of the two rims of a bicycle (Fig. 9). The packing diagram of **1a** exhibits existence of a 2D chain as a result of C–H···O interactions (Fig. S4, ESI†). O–H···S and S···S interactions (Fig. S5, ESI†) in **1a** also plays a key role in consolidating the supramolecular framework.[46]

The FTIR spectrum of **1a** reveals ample information regarding the structure of transformed cluster (Fig. 2b). It shows a peak at 3448 $cm^{-1}$ due to $\nu$(O–H) stretching vibrations and a peak near 3241 $cm^{-1}$ corresponding to $\nu(NH_2)$ stretching vibrations. The **1a** also shows a peak in the 1646 $cm^{-1}$ region, characteristic of $\nu$(C–O) and a sharp peak at 2075 $cm^{-1}$ corresponding to $\nu(SCN^-)$ binding with the central metal ion. The M–O–M group stretching vibrations were observed at 811 and 938 $cm^{-1}$ in the present cluster. The thermogram for **1a** indicates that the dimer eliminates water molecules at temperatures up to 180 °C. The weight loss of 3.5% in the first step corresponds to the exact number of six water molecules coordinated to two sodium metal ions present as proposed from the analytical data and crystal structures. In the second step, the complex eliminates thiocyanate ligands at temperatures up to 250 °C. The weight loss of 21% in this step corresponds to the exact number of eight coordinated thiocyanate ligands from the coordination sphere. In the next step, the removal of the six

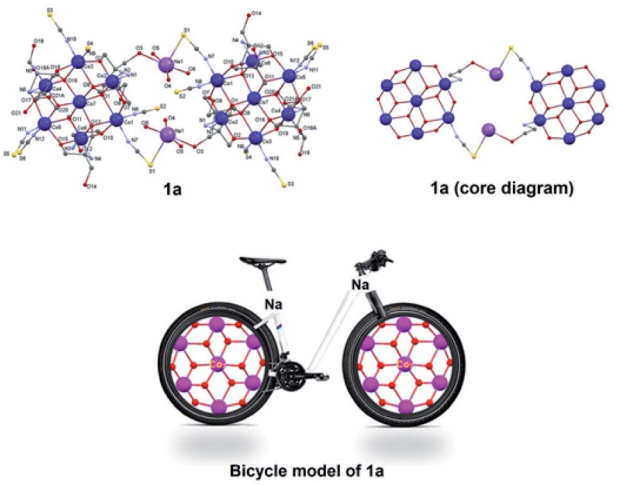


Fig. 9 Crystal structure of **1a** and core diagram of **1a** with its bicycle representation.

amino alcohol ligands along with two remaining thiocyanate ligands takes place in the temperature range 250–550 °C, with a weight loss of 28%. A further increase in the temperature up to 600 °C gives rise to the elimination of rest of the metal oxide compound from the rest of the compound with a weight loss of 24% (Fig. 2c). Further the PXRD experiment was also performed to understand the bulk purity of the crystals. The PXRD patterns are almost the same in simulated and experimental forms, corroborating the bulk purity of **1a** (Fig. 2d).

**3.4.2. DFT calculations.** Following our expertise in the DFT,[23,25,47,48] we have also performed theoretical study to get more insights about what triggers the transformation in the present complexes by adding NaSCN. We have considered a high spin surface of each cobalt center and performed DFT study.[48–53] So, we have performed DFT calculations on **1–3** and **1a** in which three cobalt centers are in +3 and four are in the +2 oxidation state. Our computed spin density plots for the high spin surface of all three complexes are shown in Fig. 2. Spin density values confirm the presence of respective unpaired electron(s) on the cobalt center with a significant delocalization (see Fig. 10).

We have studied the formation energy of complexes taking into account the monocentric cobalt system along with coordinated ligands and also substituted SCN/$H_2O$ with $H_2O$/SCN along with neighbouring cobalt centers (see Fig. 11). The computed results show that the formation energies of **2** and **3** are relatively more stable than that of **1** by 2161.0 and 3458.0 kJ $mol^{-1}$, respectively. We have again computed the formation energies, by considering a monocenter along with coordinated ligands, for **2** and **3** which are relatively more stable by 507.0 and 827.0 kJ $mol^{-1}$, respectively, than that of **1**. We have also modelled the structure by replacing the SCN by $H_2O$ at the $Co_5$ center, one of the SCN molecules by $H_2O$ at the $Co_1$, and

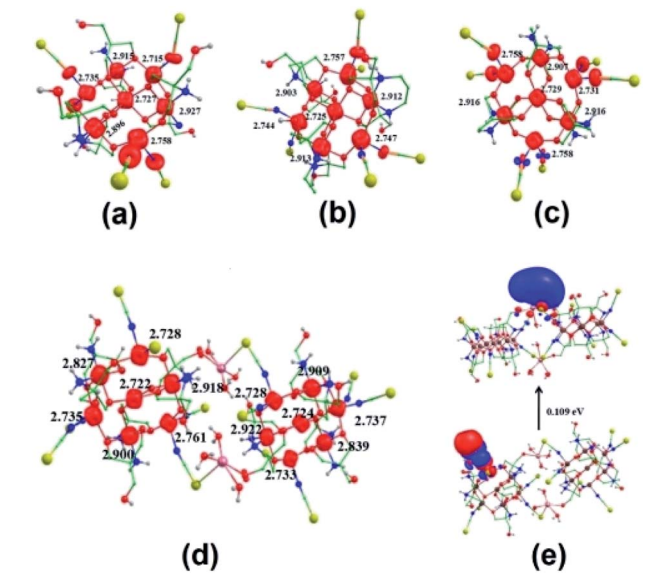


Fig. 10 Computed spin density plots of **1** (a), **2** (b) and **3** (c); computed spin density plot for **1a** (d) and HOMO–LUMO gap between the frontier molecular orbitals of **1a** (e).

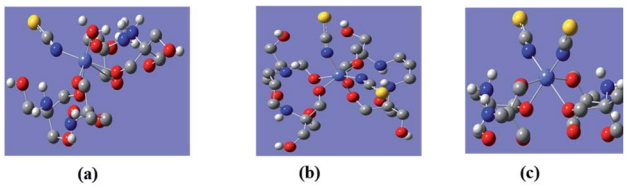


Fig. 11 Monocentric cobalt with coordinated ligands of (a) **1** (b) **2** and (c) **3**.

one SCN by $H_2O$ at each $Co_1$ and $Co_3$ center of **1** and observed that the stability of the molecule decreases in each case by 436.3, 375.7 and 977.4 kJ $mol^{-1}$, respectively. The computed bond strengths of Co–$OH_2$ and Co–SCN further show that the Co–$OH_2$ is weaker (65.8 kJ $mol^{-1}$) than Co–SCN (553.7 kJ $mol^{-1}$), which concludes that coordination of water molecules can decrease the stability of **1** and dimerization can take place at the Co–$OH_2$ center easily.

This corroborates this rare transformation dimerization of **1** into **1a.** This elucidated the reason behind the detection of SCN by **1** in the aqueous medium. For investigating why **2** and **3** do not get dimerize, we have again modelled **2** and **3** by replacing one of the SCN at a cobalt center by a water molecule and the results show that the stability of the complexes decreases by 185.6 and the 163.2 kJ $mol^{-1}$, respectively. The computed dissociation energies of Co–SCN in **2** and **3** are significantly very high, 578.3 and 588.8 kJ $mol^{-1}$, for cleaving the bonds and this prevents any dimerization in the cases of **2** and **3**, thus assuring the sensing ability of **1**. Further, the HOMO–LUMO energy gap of **1**, **2** and **3** is 2.016, 2.037 and 2.031 eV, respectively (Fig. 12). The Mulliken frontier molecular-orbital composition for **1** shows a significant charge contribution on cobalt centers (Table S4, ESI†). These significant differences in charge contributions along with the lowest HOMO–LUMO gap also support that **1** may show higher activity to a chemical transformation (recognition of thiocyanate). The spin density plot for **1a** and the HOMO–LUMO energy gap ($\Delta E$) between frontier molecular

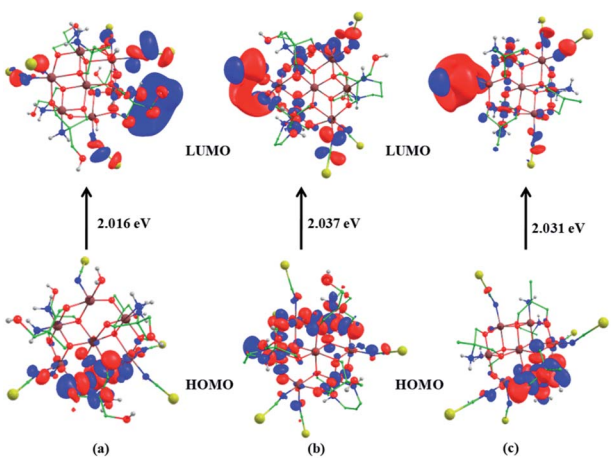


Fig. 12 HOMO–LUMO energy gap ($\Delta E$) between the frontier molecular orbitals of **1** (a), **2** (b) and **3** (c).

orbitals are also calculated and depicted in Fig. 10 and 12, respectively. It is interesting to note that the magnitude of $\Delta E$ for the $Co_{14}$ species, **1a** (2.109 eV), obtained after transformation is much lesser than that calculated for the monomeric $Co_7$ species, **1** (2.016 eV). This assures that the transformed product could be less stable and is generated in solution for a while in the form of crystals,[23,25,48] which have instantly been diffracted.

# 4. Conclusion

In summary, we report here three Co-based clusters with their complete crystallographic and theoretical analysis. **1** has been utilized as a chemosensor for the detection of thiocyanate selectively in the aqueous medium. **1** was used to detect SCN in different anions and even in very little concentration. Further, **1** can be employed to detect SCN even in real blood samples which makes this material a better cluster to detect the concentration of SCN in smokers and non-smokers. The mechanism of detection of SCN by **1** was further verified by HSAB principle, single crystal analysis, and DFT calculations. The transformation at the discrete molecular level highly depends upon the structure of the complex, its formation energy and bond energies of the sites to get transformed and other structural factors as evidenced by theoretical analysis of the present $Co_7$ cluster **1**. This is the first report of a molecular complex to sense thiocyanate forming a dimeric crystal as the ultimate product as evidenced by single crystallography. The symbiosis effect (HSAB principle) also plays a key role in controlling exchange of the coordinated ligand with the host thiocyanate. Hence, the present cluster material **1** in future could be useful as a biomarker for the detection of hazardous thiocyanate concentrations in the aqueous medium as well as in human blood samples.

# Conflicts of interest

There are no conflicts to declare.

# Acknowledgements

The authors acknowledge the financial assistance from DST FIST and UGC-DRS (SAP-II) Programs. M. S. thanks Prof. Cristopher E. Anson, Department of Chemistry, KIT, Germany, for his valuable suggestions regarding establishing the exact crystal structure of **1a**.

# References

1 M. G. Valdes and M. E. Dıaz-Garcıa, Determination of Thiocyanate within PhysiologicalFluids and Environmental Samples: Current Practice and Future Trends, *Crit. Rev. Anal. Chem.*, 2004, **34**, 9–23.

2 Y. Zhang, H. Wang and R. H. Yang, Colorimetric and Fluorescent Sensing of $SCN^-$ Based on meso-Tetraphenylporphyrin/meso-Tetraphenylporphyrin Cobalt(II) System, *Sensors*, 2007, **7**, 410.

3 R. M. Naik, B. Kumar and A. Asthana, Kinetic spectrophotometric method for trace determination of thiocyanate based on its inhibitory effect, *Spectrochim. Acta, Part A*, 2010, **75**, 1152–1158.

4 Z. Glatz, S. Novakova and H. Sterbova, Analysis of thiocyanate in biological fluids by capillary zone electrophoresis, *J. Chromatogr. A*, 2001, **916**, 273–277.

5 M. T. Ashby, A. C. Carlson and M. J. Scott, Redox Buffering of Hypochlorous Acid by Thiocyanate in Physiologic Fluids, *J. Am. Chem. Soc.*, 2004, **126**, 15976–15977.

6 S. E. Chemaly, M. Salathe, S. Baier, G. E. Conner and R. Forteza, Hydrogen Peroxide–Scavenging Properties of Normal Human Airway Secretions, *Am. J. Respir. Crit. Care Med.*, 2003, **167**, 425–430.

7 A. Afkhami, F. Soltani-Felehgari and T. Madrakian, Highly sensitive and selective determination of thiocyanate using gold nanoparticles surface decorated multi-walled carbon nanotubes modified carbon paste electrode, *Sens. Actuators, B*, 2014, **196**, 467–474.

8 M. Yu, H. Yu and R.-S. Li, Fast analysis of thiocyanate by ion-pair chromatography with direct conductivity detection on a monolithic column, *Chin. Chem. Lett.*, 2013, **24**, 1067–1069.

9 I. Demkowska, Z. Polkowska and J. Namiesnik, Application of ion chromatography for the determination of inorganic ions, especially thiocyanates in human saliva samples as biomarkers of environmental tobacco smoke exposure, *J. Chromatogr. B: Anal. Technol. Biomed. Life Sci.*, 2008, **875**, 419–426.

10 Y. Tanaka, N. Naruishi, H. Fukuya, J. Sakata, K. Saito and S.-I. Wakida, Simultaneous determination of nitrite, nitrate, thiocyanate and uric acid in human saliva by capillary zone electrophoresis and its application to the study of daily variations, *J. Chromatogr. A*, 2004, **1051**, 193–197.

11 H. Akiyama, T. Toida, S. Sakai, Y. Amakura, K. Kondo, Y. Sugita-Konishi and T. Maitani, Determination of cyanide and thiocyanate in sugihiratake mushroom using HPLC method with fluorometric detection, *J. Health Sci.*, 2006, **52**, 73–77.

12 T. Ohshima, S. Kagaya, M. Gemmei-Ide, R. W. Cattrall and S. D. Kolev, The use of a polymer inclusion membrane as a sorbent for online preconcentration in the flow injection determination of thiocyanate impurity in ammonium sulfate fertilizer, *Talanta*, 2014, **129**, 560–564.

13 Y. Zhang, H. Wang and R. H. Yang, Colorimetric and fluorescent sensing of $SCN^-$ based on meso-tetraphenylporphyrin/meso-tetraphenylporphyrin cobalt(II) system, *Sensors*, 2007, **7**, 410–419.

14 A. Banerjee, A. Sahana, S. Lohar, I. Hauli, S. K. Mukhopadhyay, D. A. Safin, M. G. Babashkinaet, M. Bolte, Y. Garcia and D. Das, A rhodamine derivative as a "lock" and SCN- as a "key": visible light excitable SCN− sensing in living cells, *Chem. Commun.*, 2013, **49**, 2527–2529.

15 J. Song, F.-Y. Wu, Y.-Q. Wan and L.-H. Ma, Ultrasensitive turn-on fluorescent detection of trace thiocyanate based on fluorescence resonance energy transfer, *Talanta*, 2015, **132**, 619–624.

16 H.-H. Deng, C.-L. Wu, A.-L. Liu, G.-W. Li, W. Chen and X.-H. Lin, Colorimetric sensor for thiocyanate based on anti-aggregation of citrate-capped gold nanoparticles, *Sens. Actuators, B*, 2014, **191**, 479–484.

17 J. Zhang, C. Yang, X. Wang and X. Yang, Colorimetric recognition and sensing of thiocyanate with a gold nanoparticle probe and its application to the determination of thiocyanate in human urine samples, *Anal. Bioanal. Chem.*, 2012, **403**, 1971–1981.

18 Z. Zhang, J. Zhang, C. Qu, D. Pan, Z. Chen and L. Chen, Label free colorimetric sensing of thiocyanate based on inducing aggregation of Tween 20-stabilized gold nanoparticles, *Analyst*, 2012, **137**, 2682–2686.

19 L. Wu, Z. Wang, S. Zong and Y. Cui, Rapid and reproducible analysis of thiocyanate in real human serum and saliva using a droplet SERS-microfluidic chip, *Biosens. Bioelectron.*, 2014, **62**, 13–18.

20 P. Pienpinijtham, X. X. Han, S. Ekgasit and Y. Ozaki, Highly sensitive and selective determination of iodide and thiocyanate concentrations using surface-enhanced Raman scattering of starch-reduced gold nanoparticles, *Anal. Chem.*, 2011, **83**, 3655–3662.

21 S. Narkowicz, E. Jaszczak, Z. Polkowska, B. Kiełbratowska, A. Kotłowska and J. Namiesnik, Determination of thiocyanate as a biomarker of tobacco smoke constituents in selected biological materials of human origin, *Biomed. Chromatogr.*, 2018, **32**, e4111.

22 M. J. Frisch, *et al.*, *Gaussian 09, revision 02*, Gaussian, Inc., Wallingford, CT, 2009.

23 A. Ansari, A. Kaushik and G. Rajaraman, Mechanistic Insights on the *ortho*-Hydroxylation of Aromatic Compounds by Non-heme Iron Complex: A Computational Case Study on the Comparative Oxidative Ability of Ferric-Hydroperoxo and High-Valent $Fe^{IV}$=O and $Fe^{V}$=O Intermediates, *J. Am. Chem. Soc.*, 2013, **135**, 4235–4249.

24 A. Ansari, P. Jayapal and G. Rajaraman, *Angew. Chem., Int. Ed.*, 2014, **53**, 1–6.

25 A. Ansari, M. Ansari, A. Singha and G. Rajaraman, Interplay of Electronic Cooperativity and Exchange Coupling in Regulating the Reactivity of Diiron(IV)-oxo Complexes towards C−H and O−H Bond Activation, *Chem.–Eur. J.*, 2017, **23**, 10110–10125.

26 S. J. Grimme, Semiempirical GGA-Type Density Functional Constructed with a Long-Range Dispersion Correction, *Comput. Chem.*, 2006, **27**, 1787–1799.

27 A. D. Becke, *J. Chem. Phys.*, 1993, **98**, 5648–5652.

28 C. Lee, W. Yang and R. G. Parr, *Phys. Rev. B: Condens. Matter Mater. Phys.*, 1988, **37**, 785–789.

29 T. H. Dunning Jr and P. J. Hay, in *Modern Theoretical Chemistry*, ed. H. F. Schaefer, Plenum, New York, 1976, vol. 3.

30 P. J. Hay and W. R. Wadt, *Ab initio* effective core potentials for molecular calculations. Potentials for the transition metal atoms Sc to Hg, *J. Chem. Phys.*, 1985, **82**(1), 270–283.

31 W. R. Wadt and P. J. Hay, *Ab initio* effective core potentials for molecular calculations. Potentials for main group elements Na to Bi, *J. Chem. Phys.*, 1985, **82**(1), 284–298.

32 W. R. Wadt and P. J. Hay, Ab initio effective core potentials for molecular calculations. Potentials for main group elements Na to Bi, *J. Chem. Phys.*, 1985, **82**(1), 284–298.

33 M. N. Ahamad, F. Sama, M. N. Akhtar, Y.-C. Chen, M.-L. Tong, M. Ahmad, M. Shahid, S. Hussain and K. Khan, A disc-like $Co_7$ cluster with a solvent dependent catecholase activity, *New J. Chem.*, 2017, **41**, 14057–14061.

34 J. A. Ibers and W. C. Hamilton, *International Tables for Xray Crystallography*, Kynoch Press, Birmingham, England, 1974, vol. 4.

35 *SMART & SAINT Software Reference manuals, Version 6. 45*, Bruker Analytical X-ray Systems, Inc, Madison, WI, 2003.

36 G. M. Sheldrick, *SADABS, software for empirical absorption correction, Ver. 2.05*, University of Göttingen, Göttingen, Germany, 2002.

37 *XPREP, version 5.1*, Siemens Industrial Automation Inc, Madison, WI, 1995.

38 (*a*) L. J. Bourhis, O. V. Dolomanov, R. J. Gildea, J. A. K. Howard and H. Puschmann, The anatomy of a comprehensive constrained, restrained refinement program for the modern computing environment - Olex2 dissected, *Acta Crystallogr., Sect. A: Found. Adv.*, 2015, **71**, 59–75; (*b*) O. V. Dolomanov, L. J. Bourhis, R. J. Gildea, J. A. K. Howard and H. Puschmann, *J. Appl. Crystallogr.*, 2009, **42**, 339.

39 M. C. Burla, R. Caliandro, M. Camalli, B. Carrozzini, G. L. Cascarano, L. De Caro, C. Giacovazzo, G. Polidori, D. Siliqi and R. Spagna, IL MILIONE: a suite of computer programs for crystal structure solution of proteins, *J. Appl. Crystallogr.*, 2007, **40**, 609–613.

40 M. Ashafaq, M. Khalid, M. Raizada, A. Ali, M. Faizan, M. Shahid and R. J. Butcher, Crystal Engineering and Magnetostructural Properties of Newly Designed Azide/Acetate-Bridged $Mn_{12}$ Coordination Polymers, *Cryst. Growth Des.*, 2019, **19**(4), 2366–2379.

41 M. Ashafaq, M. Raizada, M. Khalid, M. Shahid, M. Ahmad and Z. A. Siddiqi, Structural characterization, magnetic studies, and catecholase-like activities of Mn12 clusters, *J. Coord. Chem.*, 2018, **71**(14), 2118–2145.

42 M. S. Khan, M. Khalid and M. Shahid, Engineered $Fe_3$ triangle for the rapid and selective removal of aromatic cationic pollutants: complexity is not a necessity, *RSC Adv.*, 2021, **11**(5), 2630–2642.

43 M. S. Khan, M. Khalid and M. Shahid, A Co(II) coordination polymer derived from pentaerythritol as an efficient photocatalyst for the degradation of organic dyes, *Polyhedron*, 2021, **196**, 114984.

44 I. Mantasha, M. Shahid, H. A. Saleh, K. M. Qasem and M. Ahmad, A novel sustainable metal organic framework as the ultimate aqueous phase sensor for natural hazards: detection of nitrobenzene and F− at the ppb level and rapid and selective adsorption of methylene blue, *CrystEngComm*, 2020, **22**(22), 3891–3909.

45 D. Roy, K. Majhi, M. K. Mondal, S. K. Saha, S. Sinha and P. Chowdhury, Silicon quantum dot-based fluorescent probe: synthesis characterization and recognition of

thiocyanate in human blood, *ACS Omega*, 2018, **3**(7), 7613–7620.

46 (*a*) K. Iman, M. Shahid and M. Ahmad, A novel self-assembled Na $\{Cu_{12}Zn_4\}$ multifunctional material: first report of a discrete coordination compound for detection of $Ca^{2+}$ ions and selective adsorption of cationic dyes in water, *Dalton Trans.*, 2020, **49**(11), 3423–3433; (*b*) M. J. Frisch, *et al.*, *Gaussian 09, revision 02*, Gaussian, Inc., Wallingford, CT, 2009.

47 A. Ansari, A. Kaushik and G. C.-H. Rajaraman, Bond Activation by Metal-Superoxo Species: What Drives High Reactivity, *Angew. Chem., Int. Ed.*, 2015, **54**, 564–568.

48 S. Grimme, Semiempirical GGA-Type Density Functional Constructed with a Long-Range Dispersion Correction, *J. Comput. Chem.*, 2006, **27**, 1787–1799.

49 A. D. Becke, Density-Functional Thermochemistry. III. The Role of Exact Exchange, *J. Chem. Phys.*, 1993, **98**, 5648–5652.

50 C. Lee, W. Yang and R. G. Parr, Development of the Colle-Salvetti Correlation-Energy Formula into a Functional of the Electron Density, *Phys. Rev. B: Condens. Matter Mater. Phys.*, 1988, **37**, 785–789.

51 T. H. Dunning Jr and P. J. Hay, in *Modern Theoretical Chemistry*, ed. H. F. Schaefer, Plenum, New York, 1976, vol. 3.

52 P. J. Hay and W. R. Wadt, Ab Initio Effective Core Potentials for Molecular Calculations. Potentials for the Transition Metal Atoms Sc to Hg, *J. Chem. Phys.*, 1985, **82**, 270–283.

53 W. R. Wadt and P. J. Hay, Ab Initio Effective Core Potentials for Molecular Calculations. Potentials for Main Group Elements Na To Bi, *J. Chem. Phys.*, 1985, **82**, 284–298.